Biological imaging with nonlinear photothermal microscopy using a compact supercontinuum fiber laser source

Jinping He,[1,2] **Jun Miyazaki,**[1,2] **Nan Wang,**[1,2] **Hiromichi Tsurui,**[3] **and Takayoshi Kobayashi**[1,2,4,5,*]

[1]*Advanced Ultrafast Laser Research Center, University of Electro-Communications, 1-5-1 Chofugaoka, Chofu, Tokyo 182-8585, Japan*
[2]*JST, CREST, 5 Sanbancho, Chiyoda-ku, Tokyo 102-0075, Japan*
[3]*Department of Pathology, Juntendo University School of Medicine, Tokyo 113-8421, Japan*
[4]*Department of Electrophysics, National Chiao-Tung University, 1001 Ta Hsinchu Rd., Hsinchu 300, Taiwan*
[5]*Insitute of Laser Engineering, Osaka University, 2-6 Yamada-oka, Suita, Osaka 565-0971, Japan*

[*]*kobayashi@ils.uec.ac.jp*

Abstract: Nonlinear photothermal microscopy is applied in the imaging of biological tissues stained with chlorophyll and hematoxylin. Experimental results show that this type of organic molecules, which absorb light but transform dominant part of the absorbed energy into heat, may be ideal probes for photothermal imaging without photochemical toxicity. Picosecond pump and probe pulses, with central wavelengths of 488 and 632 nm, respectively, are spectrally filtered from a compact supercontinuum fiber laser source. Based on the light source, a compact and sensitive super-resolution imaging system is constructed. Further more, the imaging system is much less affected by thermal blurring than photothermal microscopes with continuous-wave light sources. The spatial resolution of nonlinear photothermal microscopy is $\sim$ 188 nm. It is $\sim$23% higher than commonly utilized linear photothermal microscopy experimentally and $\sim$43% than conventional optical microscopy theoretically. The nonlinear photothermal imaging technology can be used in the evaluation of biological tissues with high-resolution and contrast.

OCIS codes: (180.0180) Microscopy; (100.6640) Superresolution; (190.4870) Photothermal effects.

References and links

1. M. Tokeshi, M. Uchida, A. Hibara, T. Sawada, and T. Kitamori, "Determination of subyoctomole amount of nonfluorescent molecules using a thermal lens microscope: subsingle-molecule determination," Anal. Chem. **73**(9), 2112–2116 (2001).
2. D. Boyer, A. Maali, B. Lounis, and M. Orrit, "Photothermal imaging of nanometer-sized metal particles among scatterers," Science **297**(5584), 1160–1163 (2002).
3. S. Berciaud, L. Cognet, G. A. Blab, and B. Lounis, "Photothermal heterodyne imaging of individual nonfluorescent nanoclusters and nanocrystals," Phys. Rev. Lett. **93**(25), 257402 (2004).

#232730 - $15.00 USD Received 6 Feb 2015; revised 19 Mar 2015; accepted 19 Mar 2015; published 8 Apr 2015

4. D. Lasne, G. A. Blab, S. Berciaud, M Heine, L. Groc, D. Choquet, L. Cognet, and B. Lounis, "Single nanoparticle photothermal tracking (SNaPT) of 5-nm gold beads in live cells," Biophys. J. **91**(12), 4598–4604 (2006).
5. X. Huang, I. EI-Sayed, W. Qian, and M. EI-Sayed, "Cancer cell imaging and photothermal therapy in the near-infrared region by using gold nanorods," J. Am. Chem. Soc. **128**(6), 2115–2120 (2006).
6. B. Chithrani, A. Ghazani, and W. Chan, "Determining the size and shape dependence of gold nanoparticle uptake into mammalian cells," Nano. Lett. **6**(4), 662–668 (2006).
7. N. Lewinski, V. Colvin, and R. Drezek, "Cytotoxicity of nanoparticles," Small **4**(1), 26–49 (2008).
8. Y. Pan, S. Neuss, A. Leifert, M. Fischler, F. Wen, U. Simon, G. Schmid, W. Brandau, and W. Dechent, "Size-dependent cytotoxicity of gold nanoparticles," Small **3**(11), 1941–1949 (2007).
9. C. Goodman, C. McCusker, T. Yilmaz, and V. Rotello, "Toxicity of gold nanoparticles functionalized with cationic and anionic side chains," Bioconjugate Chem. **15**(4), 897–900 (2004).
10. I. Meglinski, and S. Matcher, "Quantitative assessment of skin layers absorption and skin reflectance spectra simulation in the visible and near-infrared spectral regions," Phys. Meas. **23**(4), 741–753 (2002).
11. K. Maxwell, and G. Johnson, "Chlorophyll fluorescence — a practical guide," J. Exp. Bot. **51**(345), 659–668 (2000).
12. J. Miyazaki, H. Tsurui, K. Kawasumi, and T. Kobayashi, "Optimal detection angle in sub-diffraction resolution photothermal microscopy: application for high sensitivity imaging of biological tissues," Opt. Express **22**(16), 18833–18842 (2014).
13. J. Miyazaki, H. Tsurui, A. Hayashi-Takagi, H. Kasai, and T. Kobayashi, "Sub-diffraction resolution pump-probe microscopy with shot-noise limited sensitivity using laser diodes," Opt. Express **22**(8), 9024–9032 (2014).
14. S. Braslavsky, and G. Heibel, "Time-resolved photothermal and photoacoustic methods applied to photoinduced processes in solution," Chem. Re. **92**(6), 1381–1410 (1992).
15. D. Lapotko, T. Romanovskaya, A. Shnip, and V. Zharov, "Photothermal time-resolved imaging of living cells," Lasers in Surgery and Medicine **31**(1), 53–63 (2002).
16. D. Nedosekin, E. Galanzha, E. Dervishi, A. Biris, and V. Zharov, "Super-resolution nonlinear photothermal microscopy," Small **10**(1), 135–142 (2014).
17. S. Thomsen, "Pathologic analysis of photothermal and photomechanical effects of laser-tissue interactions," Phtochem. Photobiol. **53**(6), 825–835 (1991).
18. J. Cross, *Pigments in Vegetables: Chlorophylls and Carotenoids* (Springer US, 1991), Chap. 2.
19. T. Udem, R. Holzwarth, and T. Hänsch, "Optical frequency metrology," Nature **416**(6877), 233–237 (2002).
20. C. Kaminski, R. Watt, A. Elder, J. Frank, and J. Hult, "Supercontinuum radiation for applications in chemical sensing and microscopy," Appl. Phys. B **92**(3), 367–378 (2008).
21. K. Shi, S. Yin, and Z. Liu, "Chromatic confocal microscopy using supercontinuum light," Opt. Express **12**(10), 2096–2101 (2004).
22. D. Wildanger, E. Rittweger, L. Kastrup, and S. Hell, "STED microscopy with a supercontinuum laser source," Opt. Express **16**(13), 9614–9621 (2008).
23. J. Dudley, G. Genty, and S. Coen, "Supercontinuum generation in photonic crystal fiber," Rev. Mod. Phys. **78**(4), 1135–1184 (2006).
24. J. Clowes, "Next generation of light sources for biomedical applications," Optik & Photonic. **3**(1), 36–38 (2008).
25. Y. N. Rajakarunanayake, and H. K. Wickramasinghe, "Nonlinear photothermal imaging," Appl. Phys. Lett. **48**(3), 218–220 (1986).
26. J. He, J. Miyazaki, N. Wang, H. Tsurui, and T. Kobayashi, "Label-free imaging of melanoma with nonlinear photothermal microscopy," Opt. Lett. **40**(7), 1141–1144 (2015).
27. S. Berciaud, D. Lasne, G. Blab, L. Cognet and B. Lounis, "Photothermal heterodyne imaging of individual metallic nanoparticles: Theory versus experiment," Phys. Rev. B **73**(4), 045424 (2006).
28. J. Valvano, J. Cochran, and K. Diller, "Thermal conductivity and diffusivity of biomaterials measured with self-heated thermistors," Int. J. Therm. **6**(3), 301–311 (1985).
29. V. Gusev, A. mandelis and R. Bleiss, "Theory of second harmonic thermal-wave generation: one-dimensional geometry," Int. J. Thermophys. **14**(2), 321–337 (1993).
30. A. Mandelis, A. Salnick, J. Opsal and A. Rosencwaig, "Nonlinear fundamental photothermal response in three-dimensional geometry: theoretical model," J. Appl. Phys. **85**(3), 1811–1821 (1999).
31. V. Kotaidis, C. Dahmen, G. Plessen, F. Springer, and A. Plech, "Excitation of nanoscale vapor bubbles at the surface of gold nanoparticles in water," J. Chem. Phys. **124**(18), 184702 (2006).
32. J. Power, "Pulsed mode thermal lens effect detection in the near field via thermally induced probe beam spatial phase modulation: A theory," Appl. Opt. **29**(1), 52–63 (1990).

1. Introduction

Photothermal (PT) microscopy (PTM) is very attractive for intact imaging with sensitivity as high as a single-molecule level [1-3]. To obtain PT images of universal biological tissues with even higher signal-to-noise ratio (SNR), noble metal nanoparticles are widely used to stain the

#232730 - $15.00 USD Received 6 Feb 2015; revised 19 Mar 2015; accepted 19 Mar 2015; published 8 Apr 2015

samples [4-6]. However, gold nanoparticles are proved to have cytotoxicity [7-9], and those with certain size and concentration can even cause cell death by apoptosis [8]. On the other hand, many organic molecules, such as melanin [10], heme proteins [10] and chlorophyll [11], absorb light but transfer most of the absorbed energy to heat. Such non-/weakly emissive organic molecules possess capabilities of being used as the probes for PT imaging without cytotoxicity.

The laser sources used in PT microscopy (PTM) are mostly CW lasers [1-3, 12, 13], while nanosecond solid-state lasers are used for the pump beam in the time-resolved [14, 15] and nonlinear PTM [16]. Compared with pulsed lasers, CW lasers are compact, cheap and stable, especially in the case of diode lasers [12, 13]. However, when a CW laser is used as the pump beam, the irradiation will continuously heat the tissue and it will never be fully cooled down. As a result, the tissue temperature increase will be additive and is apt to cause irreversible injury of the tissue even with relatively low onset temperature (40-45 $^{\circ}$C) [17]. Shorter pulses are more suitable in nonlinear PTM, in which thermal blurring is smaller for shorter pump pulse [17]. Picosecond or even shorter laser pulses are preferred in time-resolved PTM, since some processes, such as thermal field emerges within absorbing object, have relaxation time in picosecond scale [14, 15]. The absorption spectrum varies among different molecules/cells in the biological tissues, such as a relatively narrow band with a peak at 550 nm for hemoglobin in skin [10], a broad band extending from UV to near infrared for melanin [10] and structured spectrum with several peaks for chlorophyll [18]. Therefore, a laser source with a broad spectral range is necessary for imaging of different tissues.

Recently, supercontinuum (SC) pulsed sources are very attractive for their huge bandwidth and spectral flexibility, and have found applications in a variety of fields, such as optical frequency metrology [19], remote sensing [20], confocal microscopy [21] and STED microscopy [22]. The main drawback of the SC sources is the large fluctuation of pulse energy, which varies from $\sim$10 % to $\sim$80% with different parameters of pump laser source and nonlinear medium [23]. This large pulse energy fluctuation will induce relatively large optical noise, and hinder the applications in microscopy with pump-probe scheme, such as PTM, stimulated emission microscopy, stimulated Raman scattering microscopy, ground-state depletion microscopy. The weak signal intensity ($10^{-5} - 10^{-3}$ of the input probe intensity) will be buried in the large noise and induce low SNR of the images. To overcome the problem, a balanced detector can help to reduce the optical noise of probe pulse to near shot noise level [12, 13], and it opens wide application fields of SC sources in pump-probe microscopy. Recently, compact SC systems have emerged, based on a mode-locked fiber oscillator, fiber amplifier, and a photonic crystal fiber as the nonlinear medium [24]. The high spectral density ($>$1 mW/nm), huge spectral bandwidth (from visible to mid-infrared), and high repetition frequency (up to 80 MHz) and relatively small pulse energy fluctuations make the pulsed SC sources reliable solutions for biomedical imaging.

Besides the commonly used linear PT (LPT) microscopy (LPTM), a kind of nonlinear PT (NLPT) microscopy (NLPTM), in which the intensity of pump beam is modulated at frequency f and the PT signal is extracted from the probe beam with a lock-in amplifier referred to 2f, is also demonstrated in the imaging of silica windows [25] with higher contrast. Recently, the NLPTM has been applied in the imaging of mouse melanoma without staining [26], since the melanin in the melanoma acts as the probe for the imaging. The spatial resolution has been enhanced by 18 % compared with LPTM. Although more work is still needed for the application of the sub-diffraction-resolution imaging technology to more universal biological tissues, which do not have large absorption in the visible range.

In this paper, we have demonstrated the simultaneous LPT and NLPT imaging of mouse spinal cord, kidney and small intestine stained with chlorophyll or hematoxylin. This type of

#232730 - $15.00 USD Received 6 Feb 2015; revised 19 Mar 2015; accepted 19 Mar 2015; published 8 Apr 2015

organic molecules, other than the commonly used gold nanoparticle, may help to avoid the cytotoxicity and will be ideal probes for PTM. The pump and probe beams are spectrally filtered from a compact picosecond supercontinuum fiber laser source, and as a result, compact setup, small thermal blurring are expectable. The microscopic imaging technology will be useful in biological research.

2. Methods

The setup of the imaging system is shown in Fig. 1. A commercial SC fiber laser source (WL-SC400-4, Fianium, UK) is applied in the experiment providing both the pump and probe pulses. The whole spectral range of the SC is from 400 nm to 2.4 μm with the average power of $\sim$4 W. The master oscillator of the system is specified to provide 6 ps pulses, while the pulse duration of the spectral band in the visible range of the SC is measured to be $\sim$ 140 ps with a streak camera scope (C4334, Hamamatsu, Japan). The pulse-to-pulse noise level is less than 1% at 1064 nm, and it increases up to 4% in the red and up to 10% in the blue part. The repetition frequency of the system is tunable in the range of 100 kHz-40 MHz by using a pulse picker. In the experiment, the repetition frequency is fixed at the maximum value (40 MHz) for highest signal-to-noise ratio (SNR). The red part of the SC is firstly removed using a longpass dichroic mirror (DM) with a cut-on wavelength of 805 nm. Using a polarization beamsplitter (PBS), the beam with spectral range of 400-805 nm is split into two beams, from which the pump and probe pulses, with a spectral width of 10 nm and central wavelengths of 488 and 632 nm, are filtered with bandpass filters (F1,2). Two sets of half-wave plate (HWP1, 2) and polarizer (P1, 2) are used to adjust the polarizations and powers of pump and probe pulses. The intensity of the pump pulse is modulated at 30 kHz with an electro-optic modulator (EOM) (LM202P, Qioptiq, Germany). After having expanded with two lenses, the pump and probe beams are combined collinearly by a short-pass dichroic mirror (DM) with cut-off wavelength of 560 nm. A microscopy objective with NA of 0.9 and magnification of 60 is used to focus the two beams into the specimen, which is mounted on a set of piezo stages (PS) (P-622.2CL and P-622.ZCL, Physik Instrumente (PI), Germany), with a resolution better than 1 nm. The spatial overlapping and time delay between the pump and probe pulses are optimized for the largest LPT and NLPT signals. The forward propagating beam is then collected and collimated by a condenser lens (Olympus) with NA tunable from 0 to 1.4. The probe beam is spectrally filtered out by a band-pass filter with a central wavelength of 632nm. In order to eliminate the laser noise of the probe beam, an auto-balanced detector (BD) (Nirvana 2007, Newport, US) with bandwidth of 125 kHz is used to accumulate the signals. The analog signals from BD is divided into two parts with a divider, and they are set as the two inputs of the two lock-in amplifiers (LIA1, 2) (SR844, Stanford Research System, US; Model 7265, Signal Recovery, US) with reference frequency of 30 and 60 kHz, respectively. An AD/DA converter is applied to transfer the LPT and NLPT signals from LIAs to computer (PC) and send the moving command from the PC to the PS.

The samples used in the study are purchased from Artec. Inc. (Japan). The sample of mouse spinal cord is stained with chlorophyll, and the mouse kidney and small intestine are stained with hematoxylin and eosin (H&E). Since hematoxylin emits fluorescence weakly and eosin is a highly fluorescent dye, the former will act the as the effective probe for LPT and NLPT imaging.

To obtain images with high SNR, the time constant of LIAs and dwell time of the imaging are set at 10 and 20 ms, respectively. The pump and probe powers are 0.7 mW and 0.6 mW, respectively.

#232730 - $15.00 USD Received 6 Feb 2015; revised 19 Mar 2015; accepted 19 Mar 2015; published 8 Apr 2015

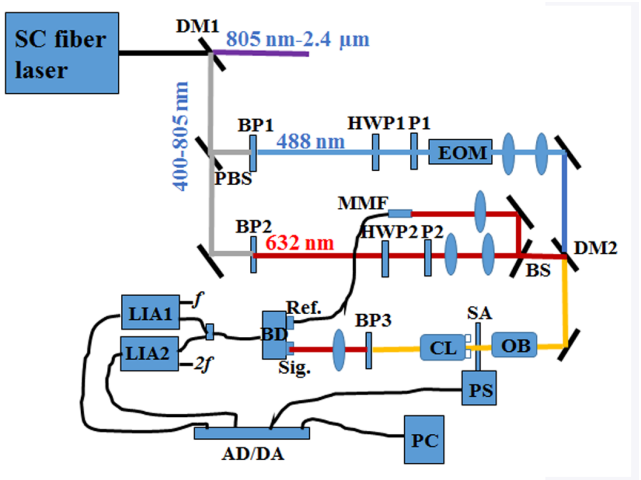

Fig. 1. Schematic diagram of the NLPT imaging system. DM1, 2: dichroic mirrors; PBS: polarization beamsplitter; BP1, 2, 3: bandpass filters; HWP1, 2: half-wave plates; P1, 2: polarizers; EOM: electro-optic modulator; BS: beamsplitter; MMF: multimode fiber; OB: objective lens; PS: piezo stage; SA: samples; CL: condenser lens; BD: auto-balanced detector; LIA1, 2: lock-in amplifiers.

3. Results and discussions

The linearity of the detection system has been discussed in [26], and the experimental results show that the signals at 2f are mainly due to the NLPT process with high pump rate with the sample of mouse melanoma. The pump power dependence of NLPT signal with the sample of mouse spinal cord is investigated to ensure the presence of nonlinearity. NLPT imaging of the same position of the sample with four different pump rate (0.12, 0.28, 0.44 and 0.60 mW) are performed with the imaging range of 10 μm $\times$ 10 μm. The maximum signals in the four images are used to demonstrate the pump power dependence of NLPT signal, and the results are shown in Fig. 2(a). A quadratic fitting is performed and it fits well with the experimental data. The quadratic power pump power dependence of NLPT signal will help to enhance the spatial resolution. Although LPT component at 60 kHz still exists due to the imperfect modulation of pump beam at 30 kHz. The heat diffusion time for LPT signal at 60 kHz is half of that at 30 kHz, and therefore may present higher spatial resolution. To check the influence of the LPT signal at 60 kHz on the spatial resolution enhancement, LPT imaging with different modulation frequency is performed. Figs. 2(b) and 2(c) show the LPT imaging of mouse kidney with modulation frequncy of pump beam at 30 and 60 kHz, respectively. The imaging range is 10 μm $\times$ 10 μm with whole pixels of 300 $\times$ 300. Fig. 2(d) shows the cross section of the position indicated by the red lines in Figs. 2(b) and 2(c). The spatial resolution is similar for the two images, while the signal intensity for the image with modulation frequency of 60 kHz (Fig. 2(c)) is about 2 times smaller than that with modulation frequency of 30 kHz (Fig. 2(b)). It means that the LPT component of the signal (due to the imperfect modulation of EOM) at 60 kHz does not give obvious contribution to the resolution enhancement, and it can be explained in the following way. The characteristic length of heat diffusion can be calculated with $r_{th} = (K/(\pi f))^{1/2}$ [27], where K the thermal diffusivity and f the modulation frequency of pump beam. With $K \sim 0.5$ W m^{-1} K^{-1} (for water and common tissue)[28], the values of r_{th} for modulation frequency of 30 and 60 kHz are calculated to be 2.3 and 1.6 μm, respectively. Both of the values are much larger than the focal spots size of the pump beam ($\sim$ 320 nm),

#232730 - $15.00 USD Received 6 Feb 2015; revised 19 Mar 2015; accepted 19 Mar 2015; published 8 Apr 2015

which means that heat diffusion will not influence the spatial resolution much with such small modulation frequency(30 and 60 kHz).

To check the reliability of LPT imaging technology, the absorption imaging of mouse kidney, detecting the energy loss of the pump beam with another similar detection system (BD + LIA), is performed simultaneously with the LPT imaging (Fig. 2(b)), as shown in Fig. 2(e). The main structures in Fig. 2(b) can be found in Fig. 2(e), althouth Fig. 2(e) shows some other different structures. The differences may be due to the absorption of pump by H&E out of focus and eosin at the focal point, which will not be efficiently detected by PT process. The contrast is much higher for PT imaging and higher axial resolution is also expectable compared with absorption imaging. An image of the same sample (different position) obtained with wide-field microscopy(Fig. 2(f)) also shows more similarities with the image obtained with PT process (Figs. 2(b) and 2(c)).

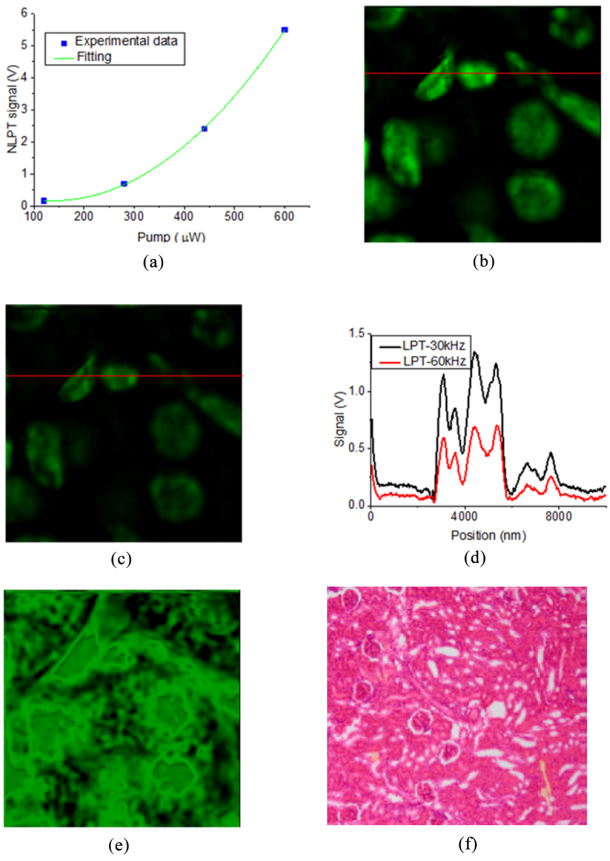

Fig. 2. LPT imaging of mouse kidney with modulation frequency of pump beam at 30 kHz (a) and 60 kHz (b), with the whole range of 10 μm $\times$ 10 μm and pixels of 300 $\times$ 300. The line profiles in (c) show the cross section of the position indicated by red lines in (a) and (b). (d) shows the absorption imaging of mouse kidney performed simultaneously with (a).

Then, the LPT and NLPT imaging of the three samples are performed. As shown in Fig. 3(a), the cross-section of mouse spinal cord is imaged with LPTM. The imaging range is 100 μm $\times$ 100 μm with the whole pixels of 200 $\times$ 200. The anterior horn and the axon bundles of spinal cord are clearly shown and distinguished. The left part of the image is anterior horn and

#232730 - $15.00 USD Received 6 Feb 2015; revised 19 Mar 2015; accepted 19 Mar 2015; published 8 Apr 2015

the right is axons from neuron. Longitudinal axons from neuron in anterior horn are running upper side. LPT (Fig. 3(b)) and NLPT (Fig. 3(c)) imaging is then performed simultaneously at a smaller scale (20 μm $\times$ 20 μm, the range marked in the red box in Fig. 3(a)) to show the detailed structures of the axon bundles. The red arrows in Fig. 3(c) denote organelles such as mitochondria and vesicles. The maximum SNR for both LPT and NLPT imaging is larger than 100. The cross sectional signal intensity of the sample at the position indicated by the red lines in Figs. 3(b) and 3(c) are shown in Fig. 3(d). They show that the sizes of the fibers are different for LPT and NLPT imaging. For example, the measured sizes of single fiber are 245 and 188 nm for LPT and NLPT imaging, respectively. It means that the spatial resolution of NLPTM is $\sim$23 % better than that of LPTM. Since the size of the point spread function (PSF) of the pump beam(488 nm) is calculated to be $\sim$330 nm, the NLPTM has a resolving ability $\sim$43 % better than conventional optical microscopy. The NLPT signal is about 40 times lower than LPT signal for the two peaks in the curves in Fig. 3(d).

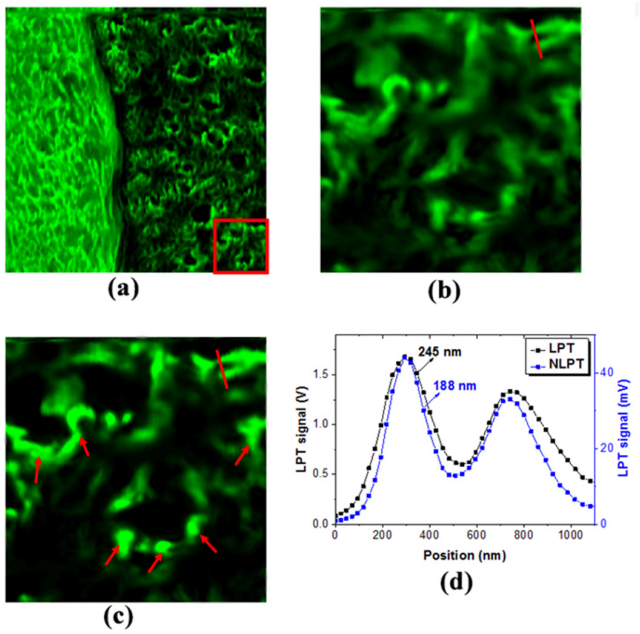

Fig. 3. LPT and NLPT imaging of cross section of mouse spinal cord. (a) LPT imaging of spinal cord with the whole range of 100 μm $\times$ 100 μm and pixels of 200 $\times$ 200. Anterior horn and axon bundle are located left and right, respectively. Strong magnification images of the range marked in the red box in are obtained with LPT (b) and NLPT (c) imaging, with the whole range of 20 μm $\times$ 20 μm and pixels of 300 $\times$ 300. The red arrows denote some organelles in the spinal cord, such as mitochondria and vesicles. The line profiles in (d) show the cross section of the position marked with red lines in (b) and (c), 245 and 188 nm for the LPT and NLPT imaging, respectively.

The images of mouse kidney obtained with LPTM and NLPTM are shown in Fig. 4. Fig. 4(a) demonstrates the LPT imaging of kidney with the range of 100 μm $\times$ 100 μm with the whole pixels of 200 $\times$ 200. The green round small bubbles are nuclei of kidney tubules. Then, LPT (Fig. 4 (b)) and NLPT (Fig. 4(c)) imaging with strong magnification is then performed simultaneously with the range of 20 μm $\times$ 20 μm, to show the detailed structures and demonstrate the spatial resolution of both of the imaging modes. The inner structures of the nuclei are clearly shown in Figs. 4(b) and 4(c). The small green dots or blocks in the nuclei show the distributions

#232730 - $15.00 USD Received 6 Feb 2015; revised 19 Mar 2015; accepted 19 Mar 2015; published 8 Apr 2015

of chromatin and heterogeneity is obviously observed. In Fig. 4(d), the cross sectional signal intensity of a nuclei, indicated by the red lines in Figs. 4(b) and 4(c), shows clear difference between LPT and NLPT imaging. The full width at half-maximum is not suited to be defined in case of the two neighbored peaks with too small distances between them. Just for a comparison, we define the sizes of the three central peaks to those of the parts above an arbitrary line, shown as the red line in Fig. 4(d). The sizes for LPT and NLPT imaging have differences of $\sim$40 %, $\sim$30 % and $\sim$40 %, respectively, for the three peaks from left to right. The ratio of LPT signal to NLPT signal is $\sim$ 120 for the three peaks in Fig. 4(d).

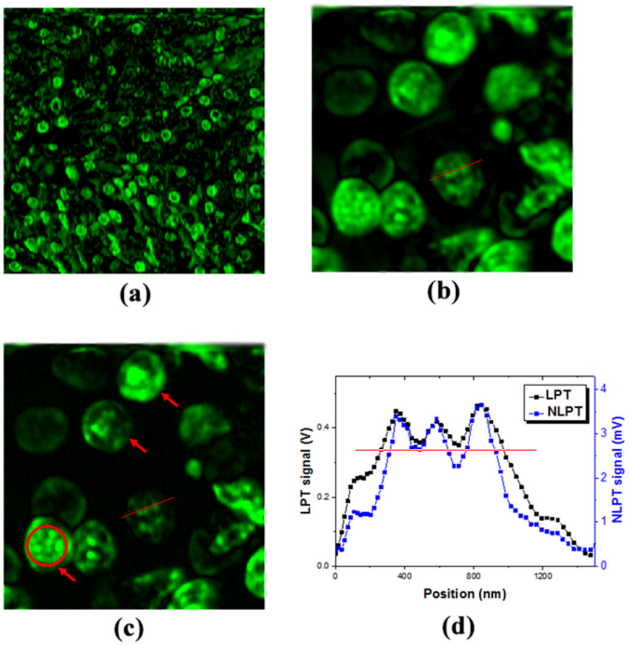

Fig. 4. LPT and NLPT imaging of mouse kidney. (a) LPT imaging of mouse kidney in the range of 100 μm $\times$ 100 μm. The green round small bulbs are nuclei of kidney tubules. (b) and (c) are LPT and NLPT images of kidney within 20 μm $\times$ 20 μm with whole pixels of 300 $\times$ 300 μm. The structure of the small green spots in nuclei, as denoted in the red cycle in (c), is due to the heterogeneity of chromatin. (d) The line profiles of the cross-sections of the nuclei indicated by the red lines in (b) and (c).

The sample of small intestine is also imaged with LPTM and NLPTM, as shown in Fig. 5. Fig. 5(a) shows the LPT imaging of small intestine with the range of 100 μm $\times$ 100 μm with the whole pixels of 200 $\times$ 200. The black holes denoted by the red arrows are intestinal microvilli, projecting from the enterocytes of its epithelium which collectively form the striated or Brush board. LPT (Fig. 5(b)) and NLPT (Fig. 5(c)) imaging of the sample is then performed with the range of 20 μm $\times$ 20 μm, as what have been done in the other two samples. The nuclei of epithelia in villi indicated by the red arrows in Figs. 5(c) are clearly imaged. Obvious enhancement of spatial resolution and contrast can be obtained for NLPTM compared with LPTM, as shown in Fig. 5. The ratio of LPT signal to NLPT signal is $\sim$ 110 for both of the two peaks in the figure, and which is closed to that of mouse kidney.

The super-resolution NLPTM allows studying biological tissues stained with organic molecules. However, in real super-resolution microscopy, it is necessary to carefully choose the molecules to enhance the NLPT signal. As shown in Figs. 3(d), 4(d) and 5(d), the ratio of

#232730 - $15.00 USD Received 6 Feb 2015; revised 19 Mar 2015; accepted 19 Mar 2015; published 8 Apr 2015

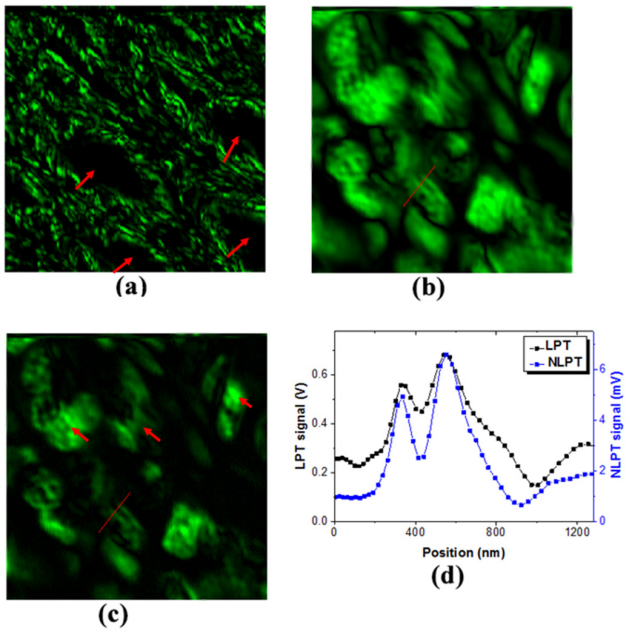

Fig. 5. LPT and NLPT imaging of medulla of mouse small intestine. (a) LPT imaging of mouse mouse small intestine in the range of 100 μm $\times$ 100 μm. The black holes denoted by the red arrows are intestinal microvilli. (b) and (c) are LPT and NLPT images of small intestine 20 μm $\times$ 20 μm with whole pixels of 300 $\times$ 300 μm. The structures denoted in the red cycle in (c) are nuclei of eptithelia in villi. (d) The line profiles of the cross-sections of the nuclei indicated by the red lines in (b) and (c).

LPT signal to NLPT signal is $\sim$ 4 time smaller for mouse spinal cord (stained with chlorophyll) than those for mouse kidney and small intestine (stained with hematoxylin), which may be due to the different absorption cross section of the two types of molecules at 488 nm. To obtain better probes for NLPT imaging, further work can be focused on the study of more such organic molecules about the absorption, heat yield and cytotoxicity.

It should be noted that the pulsed laser is needed for NLPTM. The effective confinement of thermal energy is critical for the observation of NLPT process and obtaining high NLPT signal [25, 29, 30]. Heating of the sample with pulsed laser will be completed within the pump pulse duration, while modulated CW laser requires well suited frequency of the intensity modulation. The diameter of thermal blurring can be estimated as $d_B = (4kt_B)^{1/2}$ [16], where k is the thermal conductivity and t_B is the laser pulse width (pulsed laser) or signal acquisition time (CW laser). If we set the value of t_B to be 100 ps and 10 μs for pulsed pump and CW pump, respectively, the diameter of thermal blurring with pulsed pump is $\sim 3 \times 10^3$ times smaller than that with CW laser. In case the thermal energies generated by both pulsed laser and CW laser are set to be same, the thermal energy density is $\sim 3 \times 10^{10}$ times larger for pulsed pump.

Besides the NLPTM demonstrated in the present paper (related to thermal-wave second-harmonic generation), there also are some other types of NLPTM, such as the NLPTM related to bubble generation (NLPTM-BG) [16]. The nanobubbles in NLPTM-BG can enhance the PT signal largely by nonlinear resonance process, and hence enhance the spatial resolution. The temperature needs for the nanobubble formation is higher than 100 °C [31], and it will lead to irreversible damages in the tissues [17]. The temperature increase induced in the present exper-

#232730 - $15.00 USD Received 6 Feb 2015; revised 19 Mar 2015; accepted 19 Mar 2015; published 8 Apr 2015

iment can be estimated in the following way. The temperature profile $\triangle T(r,t)$ at time t after pump pulse and at the position r from the small absorbing molecule in the sample following excitation by a laser pulse can be written as: [32]

$$\triangle T(r,t) = \frac{kE_{abs}}{\pi K((\omega_0)^2 + 4kt)} e^{-r^2/(\omega_0^2+4kt)}, \tag{1}$$

where k the thermal conductivity, E_{abs} the pulse energy absorbed by the sample, K the the thermal diffusivity, and ω_0 the 1/e radius of the guassian beam. With the parameters of $k \sim 1.3 \times 10^{-7}$ m^2/s (for water and common tissue) [28], $E_{abs} = 1.75 \times 10^{-11}$ J (the sample absorbs 10 % of the pulse energy), $K \sim 0.5$ W m^{-1} K^{-1} (for water and common tissue)[28], $\omega_0 = 300$ nm, $t = 0$ s and $r = 0$ m, we can get the temperature increase at the position of the absorber induced by a single pulse $\triangle T = 1.6 \times 10^{-5}$ °C. If the thermal loss due to thermal conduction is not considered, the temperature increase in one modulation period ($\sim 1.3 \times 10^3$ pulses heat the sample successively) is $\sim 2.1 \times 10^{-2}$ °C, and the value is far below the threshold for tissue coagulation.

4. Conclusion

NLPTM is applied in the imaging of biological tissues stained with chlorophyll and hematoxylin. Experimental results also show that this type of molecules, which absorb light but transform most of the absorbed energy into heat, may be ideal probes for LPT and NLPT imaging without toxicity. The pump and probe beams are spectrally filtered from a compact picosecond supercontinuum fiber laser source. The advantages of the application of pulsed laser in PTM has been discussed. The spatial resolution of NLPTM is ~23% higher than commonly utilized LPTM. The NLPTM presented herein is relatively universal and can be used in all the biological tissues stained with such organic aromatic molecules.

#232730 - $15.00 USD Received 6 Feb 2015; revised 19 Mar 2015; accepted 19 Mar 2015; published 8 Apr 2015